Title

Substrate topology and cognate immunity modulate antibacterial toxicity of Tae cell wall hydrolases

Authors

Atanas Radkov[1], Anne Sapiro[1], Sebastian Flores[2], Corey Henderson[3], Hayden Saunders[1], Rachel Kim[4], Steven Massa[5], Samuel Thompson[6], Chase Mateusiak[7], Jacob Biboy[8], Ziyi Zhao[1], Lea M Starita[9,10], William Hatleberg, Waldemar Vollmer[8], Alistair B Russell[11], Jean-Pierre Simorre[12], Spencer Anthony-Cahill[13], Peter Brzovic[14], Beth Hayes[1], Seemay Chou[1]*

1 Department of Biochemistry & Biophysics, University of California – San Francisco, San Francisco, CA
2 University of Miami, Miami, FL
3 InBios International, Seattle, WA
4 Pacific Northwest University of Health Sciences, Yakima, WA
5 Department of Biology, Stanford University, Stanford, CA
6 Department of Bioengineering, Stanford University, Stanford, CA
7 Computer Science Department, University of Washington in St Louis, St. Louis, MO
8 Center for Bacterial Cell Biology, Newcastle University, Newcastle upon Tyne, United Kingdom
9 Department of Genome Sciences, University of Washington, Seattle, WA
10 Brotman Baty Institute for Precision Medicine, Seattle, WA
11 Division of Biological Sciences, University of California, San Diego, La Jolla, CA
12 Université Grenoble Alpes, CNRS, CEA, IBS, Grenoble, France
13 Chemistry Department, Western Washington University, Bellingham, WA
14 Department of Biochemistry, University of Washington, Seattle, WA

*Corresponding author: seemay.chou@ucsf.edu

Abstract

Members of the bacterial T6SS amidase effector (Tae) superfamily of toxins are delivered between competing bacteria to degrade cell wall peptidoglycan. Although Taes share a common substrate, they exhibit distinct antimicrobial potency across different competitor species. To investigate the molecular basis governing these differences, we quantitatively defined the functional determinants of Tae1 from *Pseudomonas aeruginosa* PAO1 using a combination of nuclear magnetic resonance (NMR) and a high-throughput *in vivo* genetic approach called deep mutational scanning (DMS). As expected, combined analyses confirmed the role of critical residues near the Tae1 catalytic center. Unexpectedly, DMS revealed substantial contributions to enzymatic activity from a much larger, ring-like functional hot spot extending around the entire circumference of the enzyme. Comparative DMS across distinct growth conditions highlighted how functional contribution of different surfaces is highly context-dependent, varying alongside composition of targeted cell walls. These observations suggest that Tae1 engages with the intact cell wall network through a more distributed three-dimensional interaction interface than previously appreciated, providing an explanation for observed differences in antimicrobial potency across divergent Gram-negative competitors. Further binding studies of several Tae1 variants with their cognate immunity protein demonstrate that requirements to maintain protection from Tae activity may be a significant constraint on the mutational landscape of *tae1* toxicity in the wild. In total, our work reveals that Tae diversification has likely been shaped by multiple independent pressures to maintain interactions with binding partners that vary across bacterial species and conditions.

Introduction

Bacteria live in dense polymicrobial communities where competition for nutrients and space impacts survival[1]. To combat neighboring rivals, some Gram-negative bacteria use a contact-dependent toxin delivery system called the Type 6 secretion system (T6SS)[2,3] that injects a cocktail of effectors from the donor cell directly into nearby recipient cells[4–6]. A bacterium's T6S arsenals include several types of protein effectors with distinct activities that each compromise essential cellular pathways or components, such as recipient peptidoglycan (PG) or membranes. Although many T6S bacteria deploy similar toxins, interbacterial outcomes can vary considerably depending on the bacterial species engaged in T6S-mediated competition[7,8]. The molecular basis of this organism-level specificity of interbacterial T6SSs remains poorly understood.

A potential source of specificity could be the T6S-delivered toxins themselves[9]. T6S toxins can belong to large superfamilies comprised of diverse homologs. One such example is the T6S amidase effector (*tae*) superfamily[7]. The *tae*s encode hydrolase enzymes that induce recipient cell lysis by breaking down the major structural component of bacterial cell envelopes, PG[5]. Tae toxins are known to be structurally and biochemically diverse[10]. Given that targeted PG substrates can also vary in a species-dependent manner[11], such diversity could potentially impact toxin antibacterial specificity. Tae toxins divide into four phylogenetically distinct subfamilies (Tae1-4)[7] that hydrolyze different amide bonds within PG, and toxins within the same subfamily can have unique PG compositional preferences.[10]

These observations raise the possibility that T6SS organismal specificity may be linked, in part, to the biochemical diversity of delivered toxins. Such a model would predict that physiological features of recipient microbes may have driven divergent evolution of T6S effector diversity. To address this hypothesis, a quantitative, molecular understanding of T6S effector specificity is needed. However, comprehensive functional analyses are challenging for toxins such as the Taes, given that they act on cellular substrates with complex, three-dimensional structures *in vivo*. In cells, PG is a cross-linked macromolecule that forms a contiguous, mesh-like network that is structurally heterogeneous, insoluble, and dynamically regulated[12,13]. These features are not well captured through *in vitro* functional studies that necessarily focus on soluble PG fragments.

To probe Tae–cell wall interactions in a physiologically relevant context, we developed a high throughput genetic approach known as deep mutational scanning (DMS)[16] that surveys the entire Tae enzyme for functional determinants of toxicity in live *Escherichia coli* cells. We focused on Tae1 from the common soil bacterium *Pseudomonas aeruginosa*, which is known to interact with a wide range of microbes, including *E. coli*. We found that an extended surface across the entire Tae1 enzyme is important for mediating *in vivo* degradation of cell walls. Furthermore, we present evidence that Tae1 functional determinants can be quite distinct depending on the compositional context of PG. Finally, we discovered that the evolutionary potential for Tae1 potency against a broad range of cell wall types may be constrained by orthogonal functional requirements, such as Tae1 interactions with its cognate immunity protein during T6S-mediated competition.

RESULTS

Deep mutational scanning identifies determinants of Tae1 function *in vivo*

To understand how sequence diversity within the Tae protein superfamily impacts interbacterial toxicity, we must first probe how each amino acid residue contributes to Tae function. Biochemical assays of Tae protein binding to and degradation of peptidoglycan (PG) use isolated, purified sacculi[10], which differ from the turgor-stretched PG layer in the periplasm of living cells. Thus, these assays likely identify only a subset of determinants that govern how Tae engages with PG *in vivo*. To define comprehensively and quantitatively all the amino acid residues in Tae that are important for its function *in vivo*, we developed a DMS experiment in live bacterial cells that allows us to examine the contributions of amino acid substitutions at every Tae residue in a physiologically relevant context.[14,15]

We adapted a DMS approach[16,17] to study the Tae1 protein from *P. aeruginosa*, which is injected into *E. coli* and leads to cell lysis (**Figure 1A**). We based our screen on a lysis assay that measures the toxic effects of Tae1 on *E. coli* when it is ectopically expressed in the periplasm, which contains the PG[10]. Periplasmic expression of wild-type Tae1 ($Tae1^{WT}$), but not catalytically inactive Cys30Ala Tae ($Tae1^{C30A}$), results in rapid cell lysis upon induction due to osmotic stress resulting cell wall degradation by the toxin. Cells expressing $tae1^{WT}$ are depleted from the population faster than cells expressing inactive Tae1 (**Figure 1B**). Mutations that increase or decrease the rate of Tae1-induced lysis can be identified by sequencing and analyzing plasmid copy numbers in the population over time.

We generated a barcoded *tae1* plasmid library for massively parallel screening in *E. coli* (**Figure 1C**). Mutations were introduced by error-prone PCR, and library diversity was characterized by sequencing. We focused our analysis on copies of *tae1* that had a single mutation. In total, there were 902 different Tae1 variants, which encompassed at least one amino acid substitution at every position in the 154-residue protein. To ensure Tae1 delivery to the bacterial cell wall, we

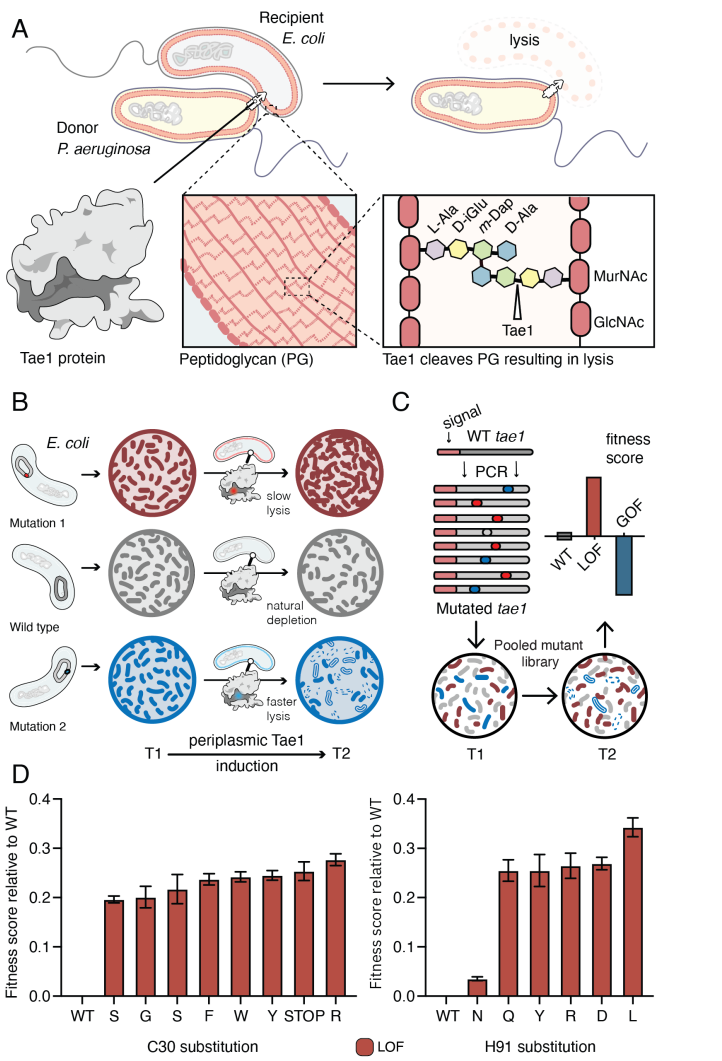

Figure 1. Deep mutational scanning identifies amino acid residues important for Tae1 function *in vivo*. (A) Illustration of the function of the *P. aeruginosa* Tae1 toxin in lysis of *E. coli*. The donor *P. aeruginosa* cell injects Tae1 into the periplasm of the recipient *E. coli* cell. Tae1 cleaves cell wall PG at the cleavage site, resulting in cell lysis. (B) Illustration of lysis assays expressing Tae1 in the periplasm of *E. coli*. When wild-type Tae1 is expressed, cells are depleted over time (gray). When a loss-of-function mutation such as $Tae1^{C30A}$ is expressed, cells grow normally (red). When a gain-of-function mutation is expressed, cells are depleted more quickly over time (blue). T1 = time 1, T2 = time 2. (C) Schematic of deep mutational scanning screen for functional determinants of Tae1. A library of Tae1 mutants was transformed into *E. coli* and periplasmic expression of the mutant toxins was induced. The number of mutant cells remaining at T2 compared to the number at T1 yield a fitness score for each variant. Increased fitness indicates loss-of-function mutations in Tae1, which decrease cell lysis, whereas decreased fitness indicates gain-of-function mutations, which increase lysis. (D) DMS-derived relative fitness scores for all substitutions in the library at the Cys30 and His91 positions. Data shown are means +/- standard deviation, n = 3. DMS experiment in M9 media was repeated 3 independent times, each time with at least.3 technical replicates.

expressed the variants as fusion proteins with N-terminal periplasm-targeting *pelB* signal sequences. We transformed *E. coli* (BW25113) grown in M9 minimal media with our *tae1* library and sequenced plasmid barcodes, both before and two hours after library induction (**Figure 1C**). Tae1-dependent lytic effects were quantified by using the DMS analysis pipeline Enrich2[17], which calculates output-to-input ratios for individual variants, yielding fitness scores that are normalized to wild type (**Supplemental Table 1**). In our assay, the fitness score reflects a difference in the antibacterial capacity of the Tae1 variant *in vivo* when compared to the wild type: relative enrichment of a variant indicates reduced Tae1-dependent cell death or loss-of-function (LOF) and yields a positive fitness score, whereas relative depletion of a variant indicates increased cell death or gain-of-function (GOF) and yields a negative fitness score.

To validate our approach, we examined the canonical catalytic dyad residues of Tae1 to assess whether our screen accurately identified known functional determinants. Any substitutions of these catalytic residues, Cys30 and His91, should inhibit enzyme activity and lead to LOF. As anticipated, all non-synonymous amino acid changes at these sites resulted in increased fitness scores, indicating their crucial roles in Tae1 toxicity (**Figure 1C and D**) and confirming that the DMS screen was indeed selecting *in vivo* functional determinants of Tae PG-degrading toxicity.

DMS identifies functional hotspots extending around the surface of Tae1

To obtain a global view of the amino acid residues in Tae1 that affect fitness in our screen, we generated an averaged sequence-function map of variant fitness scores (**Figure 2A**). The majority of all unique Tae1 protein variants (54%) were LOF variants with positive fitness scores, whereas only 6% were GOF variants. To determine the functional role of each residue of Tae1, we collapsed and averaged scores across all substitutions at each Tae1 site (**Figure 2A**) and superposed these onto the three-dimensional structure of Tae1 (**Supplemental Figure 1**). For some Tae1 residues, position averages obscured how the degree or direction of functional change depended greatly on the specific amino acid change introduced. Therefore, we used *k*-means clustering, a statistical method for analyzing DMS data[18], to classify Tae1 residues in an unbiased way into one of four categories: residues where mutations generally decreased cell lysis (LOF^{clus}), those where mutations generally increased cell lysis (GOF^{clus}), those where mutations had variable effects on lysis (mixed), and those where mutations had little to no effect (tolerant). The vast majority of residues were categorized as

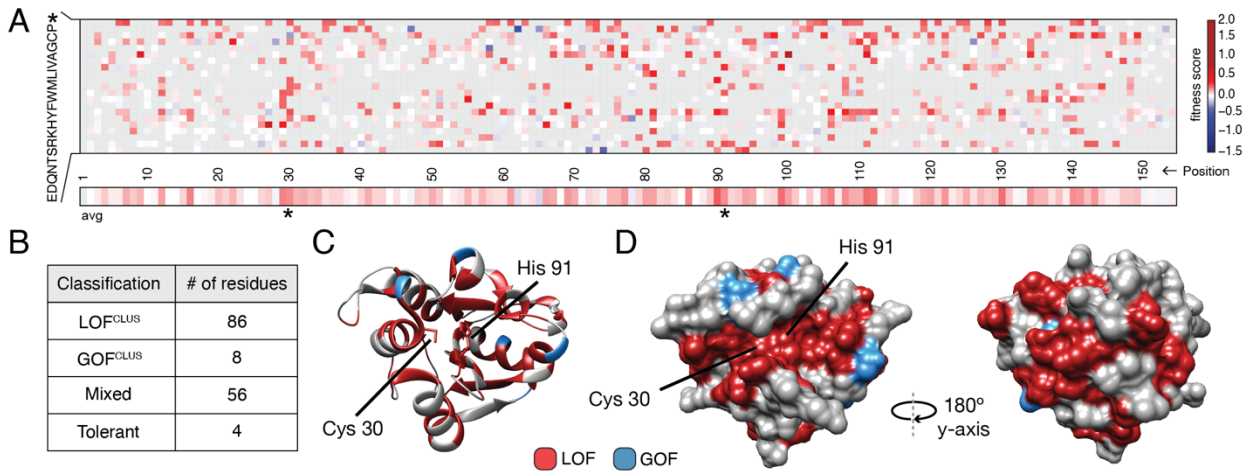

Classification	# of residues
LOF^{CLUS}	86
GOF^{CLUS}	8
Mixed	56
Tolerant	4

Figure 2. DMS identifies functional hotspots extending around the surface of Tae1. (A) Heatmap representation of fitness scores relative to wild-type Tae1 for all mutations in DMS. Each amino acid position is represented on the x-axis, and each possible amino acid substitution is represented on the y-axis, * = stop codon. Each box represents the average fitness score of three replicate experiments. The average fitness score of all substitutions at each residue is depicted across the bottom row. Catalytic residues Cys30 and His91 are indicated with asterisks. Variants in grey were not present in our library. (B) Results of *k*-means clustering of DMS data. Based on fitness effects, each residue of Tae1 was labelled loss-of-function (LOF^{CLUS}), gain-of-function (GOF^{CLUS}), mixed, or tolerant. (C) Ribbon diagram of Tae1 structure. LOF^{CLUS} residues are shown in red, GOF^{CLUS} residues are shown in blue, and all other residues are in gray. The catalytic residues of Tae1 (Cys30 and His91) are indicated. Mutations in the enzyme core lead to loss-of-function phenotypes. (D) Functional residues on the surface of Tae1. The catalytic surface of the enzyme is shown on the left and the opposite surface, after 180-degree rotation, is on the right. Color code as in part C. LOF^{CLUS} mutations are located in large areas of the surface on both sides of the enzyme, and most GOF^{CLUS} mutations are also found on the surface. See also supplemental figure 1.

either LOF^{clus} (56%) or mixed (36%), and fewer were categorized as GOF^{clus} (5%) or tolerant (3%) (**Figure 2B**). We mapped these classifications onto the Tae1 structure and found, consistent with other mutational studies, a large majority of buried residues (78%) including the catalytic residues, were categorized as LOF^{clus} (**Figure 2C**). Residues on the enzyme surface, by contrast, were a mix of categories including most of the GOF^{clus} residues.

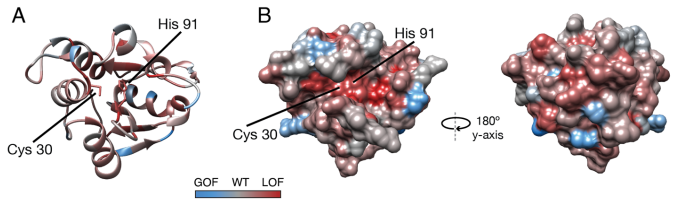

Figure S1. Average fitness score across each residue. (A) Ribbon diagram and (B) surface diagrams of fitness scores when averaging scores for all substitutions at each residue. Red residues indicate loss-of-function on average and blue residues indicate gain-of-function on average. Cys30 and His91 of the active site are indicated.

We anticipated that only surface residues within or near to the catalytic cleft would show loss-of-function phenotypes. Instead, we found that many surface-exposed residues more distant from the catalytic cleft were also categorized as LOF^{clus} (**Figure 2D**). Indeed, a zone of LOF^{clus} residues forms a ring around the entire enzyme, suggesting a more distributed set of surfaces may play key roles in cell lysis *in vivo* than was predicted by *in vitro* studies[10]. Many of the surface LOF^{clus} residues that our screen indicates are crucial for cell lysis *in vivo* are poorly conserved across the *tae1* superfamily[10]. We posit that while these mutations are LOF when applied to *E. coli* sacculi, divergent bacterial physiologies *in situ* may instead drive diversification of this extended surface.

Tae1 surfaces distal from catalytic core mediate binding and hydrolysis of cell wall network

Our DMS results suggested surfaces outside the Tae1 catalytic core are functionally important. We observed that several of these distal surface LOF^{clus} sites encoded serine and glycine residues, which have been previously implicated in sugar-binding[19,20]. Thus, it is possible that the distal LOF^{clus} surfaces are important for interacting with the glycan chains of PG. Alternatively, these distal surfaces could mediate Tae1 interactions with surrounding, untargeted peptide stems within the PG network. To validate that these residues play a role in Tae1 function, we chose nine LOF^{clus} variants distributed across the Tae1 surface (**Figure 3A**) and manually assayed their individual effects through *E. coli* lysis assays (**Figure 3B and Supplemental Figure 2**). We focused mainly on serine and glycine residues and introduced the most conservative substitutions represented in the screen (Alanines or Serines, respectively).

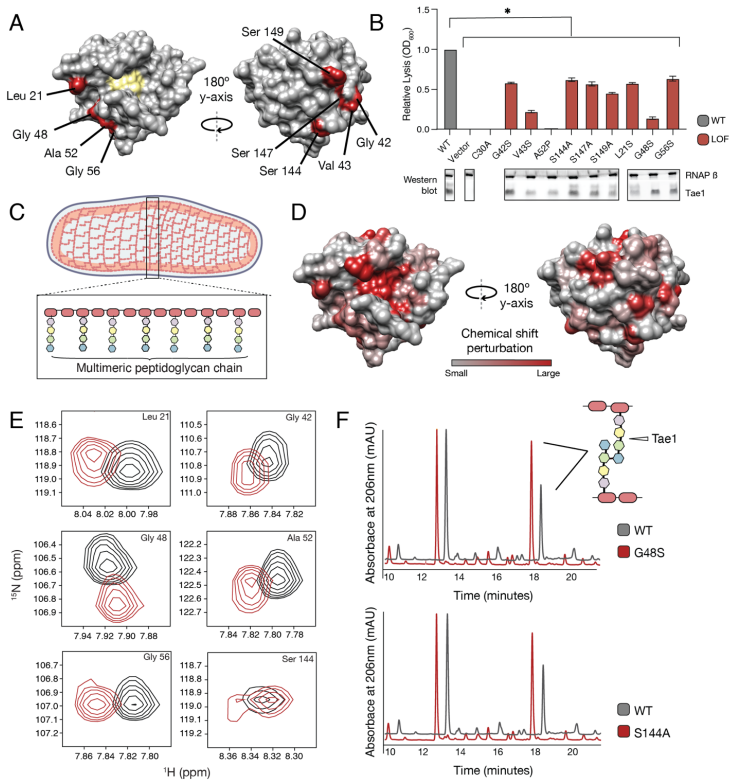

Figure 3. Tae1 surfaces distal from catalytic core mediate binding and hydrolysis of cell wall network. (A) Nine distal residues on Tae1 that had loss of function phenotypes. The catalytic core is highlighted in yellow. (B) Lysis assays measuring relative lysis of *E. coli* expressing wild-type Tae1 (WT), negative controls (vector and C30A) and loss-of-function single amino acid substitutions (G42S, V34S, A52P, S144A, S149A, L21S, G48S, G56S). Data shown are means +/- standard deviation, n = 3, * $p < 0.05$. Lysis experiment was repeated 3 independent times, each time with at least.3 technical replicates. Western blots below show the beta subunit of RNA polymerase (RNAP β) and Tae1 proteins in each assay. All variants and controls showed reduced lysis when compared to wild-type Tae1. (C) Schematic of the multimeric glycan chains used as the substrate in NMR experiments. (D) CSPs calculated from NMR spectra of Tae1 with or without multimeric PG chains mapped onto the Tae1 surface structure. Numerous residues on both sides of the Tae1 display CSPs consistent with direct substrate interactions. (E) ^{1}H-^{15}N Best-Trosy NMR spectra from Tae1 alone (black) and Tae1 incubated with multimeric peptidoglycan chains (red) for six residues from A that show CSPs. Residues distal from the Tae1 active site show shifts indicative of interactions with PG. Numerous residues display CSPs consistent with direct substrate interactions. (F) HPLC traces showing degradation of peptidoglycan in the presence of wild type (black, WT) or mutant (red) Tae1 *in vitro*. Arrows indicate peaks containing the peptide stem that can be cleaved by Tae1. Mutant Tae1 (S144A and G48S) cleaves peptidoglycan less well than wild-type Tae1 (29.1 +/- 3.2% and 36.4 +/- 4.2% less PG., respectively) See also supplemental figure 2, 3, 4.

Consistent with DMS results, all nine variants showed significantly less lytic activity than Tae1^{WT} (**Figure 3B**).

LOF phenotypes could stem from a variety of mechanisms, including reduced Tae1 protein expression, disruption of protein folding or stability, or direct inhibition of Tae1 PG binding or hydrolysis. To rule out expression and possibly stability-dependent effects, we performed Western blot analyses to measure protein levels of Tae1 variants expressed in *E. coli* (**Figure 3B**). We found that all variants were expressed; five substitutions did not exhibit major visible decreases in protein levels (G42S, S144A, S147A, G48S, G56S). Our results led us to hypothesize that these five surface substitutions may play direct roles in Tae1–PG interactions.

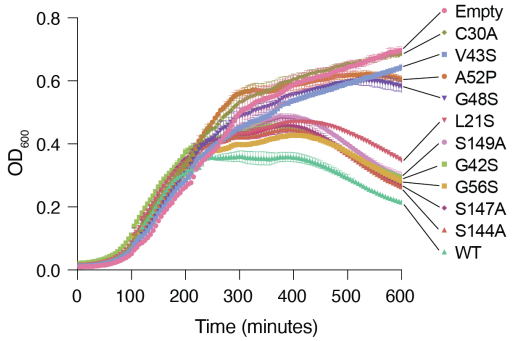

Figure S2. Lysis assay growth curves. Cell growth as measured by OD_{600} for wild type Tae1 (WT), negative controls (Empty, C30A), and the nine distal residues on Tae1 in Figure 3B. Expressing Tae1 proteins containing the nine distal residue substitutions decreases cell lysis, suggesting these are loss-of-function residues.

We hypothesized that an extended surface of Tae1 may be required for substrate binding and hydrolysis *in vivo*. Given that Tae1 likely engages with larger and even sometimes insoluble fragments of PG within the intact cell wall, we conducted a series of *in vitro* biochemical assays of LOF^{clus} variants using either intact PG sacculi or fragments that encompass more than the minimal peptide region. To address whether distal surfaces of Tae1 bind PG, we experimentally mapped Tae1 binding sites by two-dimensional (2D) nuclear magnetic resonance (NMR) using ^{15}N-labeled, catalytically inactive Tae1^{C30A} (Tae1^{N15}) in complex with larger, soluble fragments of PG. Backbone ^{13}C, ^{15}N, and ^{1}HN NMR resonances of Tae1 (>89% complete) were assigned using conventional heteronuclear techniques[21]. To prepare larger PG fragments for binding experiments, we digested *E. coli* cell wall sacculi using another Tae superfamily member (Tae3 from *Salmonella* Typhi)[7], which hydrolyzes peptide crosslinks resulting in long multimeric PG fragments that include both Tae cleavage sites and intact glycan chains (**Figure 3C**) with an average length range of 10Å to over 300Å (1 to over 30 dimeric units)[22].

To map enzyme residues that bind cell wall substrate, we compared NMR spectra of Tae1^{N15} alone or in the presence of digested multimeric PG (**Supplemental Figure 3**). Observed spectral differences allowed us to identify and quantitate chemical shift perturbations (CSPs) across the protein, which serve as indicators of residues involved in direct substrate interactions[19,20]. Mapping these shifts onto the Tae1 structure, we observed CSPs for residues located within the catalytic core as well as for a variety of both buried and exposed residues outside of the core (**Figure 3D**). While CSPs for buried residues could be due to interaction-dependent enzyme conformational or dynamical changes[23], contiguous clusters of CSPs localized to the protein surface are suggestive of Tae1–PG binding. Such putative binding regions extended all the way to surfaces on the protein face opposite of the catalytic core. In fact, we identified shifts in six of the validated LOF^{CLUS} residues: Leu21, Gly42, Gly48, Ala52, Gly56, and Ser144 (**Figure 3E**), suggesting that these residues are necessary for Tae1-induced lysis because they bind PG.

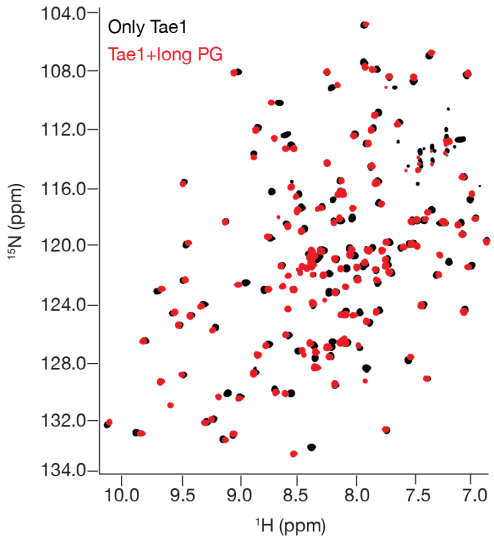

Figure S3. ^{1}H-^{15}N Best-Trosy NMR spectra of Tae1 with and without multimeric PG. NMR spectra from Tae1 alone (black) and Tae1 incubated with multimeric peptidoglycan chains (red). Numerous residues display CSPs consistent with direct substrate interactions.

To determine if these functional distal residues that bind PG are also required for hydrolysis, we focused our studies on two highly expressed variants, Tae1^{S144A} and Tae1^{G48S}, for which we expressed recombinant forms and purified**.** Size exclusion chromatography analysis of these variants showed similar elution volumes and apparent hydrodynamic radii compared to Tae1^{WT}. We then conducted degradative assays with PG sacculi purified from *E. coli*. Tae enzymes were incubated with PG sacculi, and the resulting fragments were quantitatively assessed using high-performance liquid chromatography (HPLC, **Figure 3F**). Tae1^{S144A} and Tae1^{G48S} cleaved 29.1 +/- 3.2% and 36.4 +/- 4.2% less PG, respectively, than observed for the wild-type enzyme. Despite being relatively far from the active site, these amino acid substitutions decreased Tae1 activity. Together, these data reveal that numerous sites distributed around the Tae1 surface physically interact with PG, and that these distal interaction sites are important for cell wall-degrading toxicity *in vivo*. Moreover, these results suggest our DMS-based approach can faithfully uncover novel and unexpected functional determinants *in vivo*, providing important clues to evolutionary pressures that may be acting on *tae1*.

The functional landscape of Tae1 is sensitive to PG differences

Our results point to a model in which Tae1 might interact with more structures of PG outside of the catalytic site, and these interactions are important for *in vivo* toxicity. This model predicts that Tae enzymes are sensitive to differences in cell wall architecture, and broad changes to PG composition

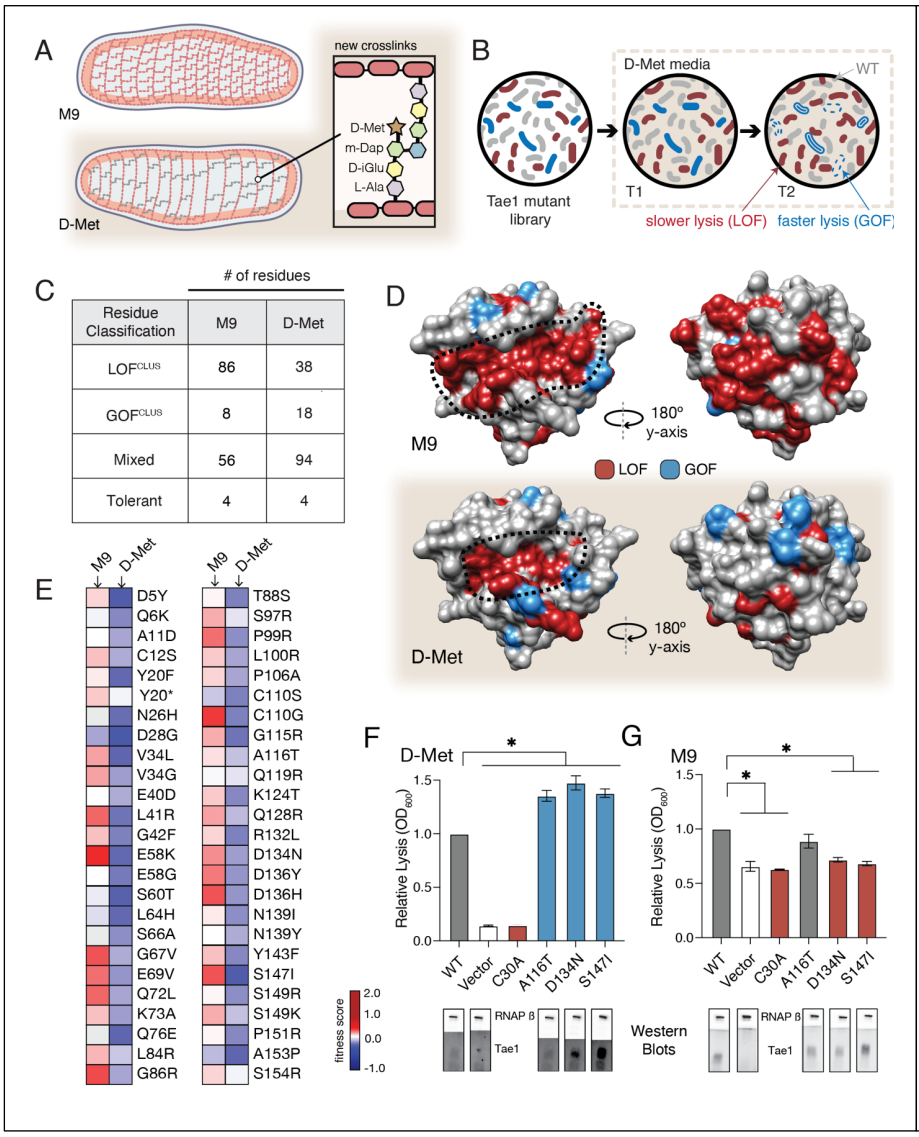

Figure 4. The functional landscape of Tae1 is sensitive to cell wall differences. (A) Cartoon illustration of cells grown in media containing D-Met showing altered PG architecture. D-Met becomes incorporated into the peptide stems and there are overall fewer crosslinks in the macromolecule. (B) Schematic of the deep mutational scanning experiments performed in media containing D-Met. DMS was completed as in Figure 1 with media containing D-Met. (C) Number of residues classified as each of the four cluster types in D-Met DMS screen. The functional classification of residues is dramatically changed from the original screen. (D) DMS-derived loss- and gain-of-function residues mapped onto the surface structure of Tae1 from the initial screen (left) and the D-Met screen (right). Compared with regular media, there were fewer loss-of-function and more gain-of-function residues in the presence of D-Met on both the catalytic face and back of the enzyme. (E) Heatmap representing average fitness scores for the top 50 GOF individual amino acid substitutions in D-Met and M9 media. n = 3. DMS in D-Met media was repeated 3 independent times, each time with at least 3 technical replicates. The majority of the GOF substitutions in D-Met are condition specific. (F) Lysis assays with wild-type Tae1, empty vector and catalytically inactive Tae1^{C30A} as negative controls, and 3 gain-of-function Tae1 variants (A116T, D134N, S147I). Data are means +/- standard deviation, n = 3, * $p < 0.05$. Lysis experiment was repeated 3 independent times, each time with at least.3 technical replicates. Western blots below measure Tae1 protein expression with RNAP as a control. All three gain-of-functions from DMS show increased lysis phenotype in individual lysis assays. (G) Lysis assays with the same Tae1 variants as in F but in M9 media. Western blots below measure Tae1 protein expression with RNAP as a control. The three D-Met GOF substitutions are condition specific. See also supplemental figure 5.

would alter Tae1–PG interactions. We hypothesized that such alterations could be captured by comparative DMS analysis across different screening conditions. To address this hypothesis, we conducted a second DMS screen in *E. coli* grown in the presence of D-methionine (D-Met), a condition known for inducing major featural changes in cell wall composition and organization (**Figure 4A**). Specifically, cell walls of *E. coli* grown in the presence of D-Met (*E. coli*^{DMet}) have generally reduced PG density and fewer modified PG crosslinks relative to cell walls of *E. coli* grown in the absence of D-Met[24,25]. We verified these trends by HPLC analysis, and we confirmed that Tae1 maintained its ability to cleave this distinct cell wall type *in vitro* (**Supplementary Figure 4**).

We performed the same suite of DMS analyses for the second screen as for the first (**Figure 4B**) and found that the calculated fitness landscape shifted dramatically. Approximately 50% fewer residues were categorized as LOF^{clus} (38/86), while the number of mixed residues increased (94/56) as did the number of GOF^{clus} residues (18/8). The number of tolerant residues did not change (4 in both) (**Figure 4C**). Overall, 58% of residues were classified differently than in our initial screen in M9 media. We mapped the LOF^{clus} and GOF^{clus} residues onto the Tae1 structure (**Figure 4D**). We also saw that the previous ring-like band of LOF^{clus} determinants emanating from the catalytic groove was greatly diminished in *E. coli*^{DMet}. Given that our biochemical experiments suggest these sites are important for extended PG-binding, we hypothesize that such contact interfaces may be less functionally critical in cellular conditions where the cell wall matrix is more loosely packed around the enzyme. Alternatively, these changes could be indirectly due to other metabolic or physical changes to the cell under D-Met growth conditions. Overall, our comparative screening approach revealed that compositional changes to PG dramatically alter the functional landscape of Tae1, suggesting these variants are sensitive to differences in cell wall architecture.

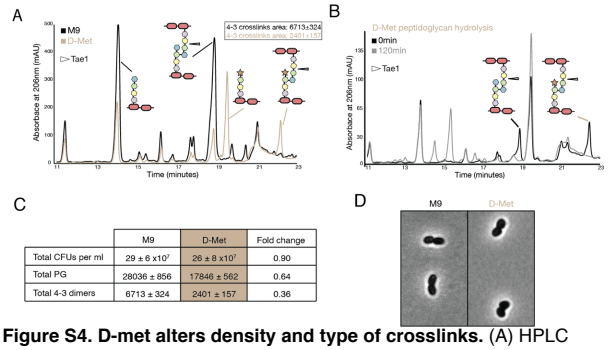

	M9	D-Met	Fold change
Total CFUs per ml	$29 \pm 6 \times 10^7$	$26 \pm 8 \times 10^7$	0.90
Total PG	28036 ± 856	17846 ± 562	0.64
Total 4-3 dimers	6713 ± 324	2401 ± 157	0.36

Figure S4. D-met alters density and type of crosslinks. (A) HPLC traces comparing peptidoglycan from cells grown in either M9 and D-met media. (B) HPLC traces showing Tae1 still degrades peptide crosslinks containing D-met. (C) Summary of PG differences between M9 and D-met media. (D) There are no major morphological changes in the presence of D-met.

The *E. coli*^{DMet} DMS screen also yielded a larger and distinct set of top-performing GOF^{clus} variants with amino acid substitutions that localized to both the catalytic groove and opposing faces of Tae1. When we compared fitness scores for the GOF^{clus} variants from the D-Met screen to the initial M9 screen, we found that only a small subset of substitutions showed similar effects across both conditions (**Figure 4E**). Condition-specific phenotypes suggests that Tae1 toxicity *in vivo* is highly context-dependent and optimizable for specific PG forms. To test this hypothesis, we conducted lysis assays in D-Met and M9 media for three GOF variants uniquely identified in the D-Met screen (**Figure 4F and G**). All three substitutions increased cell lysis in *E. coli* grown in D-Met but not M9 minimal media. For two of the variants, Asp134Asn and Ser147Ile, the increase in lysis may be due to higher expression levels based on Western blot analysis (**Figure 4F and G**). Together, these results suggest Tae enzymes could possibly be engineered to target specific bacteria with certain cell wall structures. Given that the structure and composition of PG varies across bacterial species, our results also potentially point to a selective pressure underlying natural sequence-based diversity in the Tae1 superfamily. Namely, cell wall features associated with particular rival species a given bacterium must antagonize may drive evolved substrate specificity differences in interbacterial competition toxins such as the Tae enzymes.

A hyperactive variant of Tae1 is naturally encoded by other *tae* homologs

A number of context-independent Tae1 variants that significantly out-performed wild-type enzyme across both DMS conditions were also identified through our comparative approach. We were

349 particularly struck by one variant, Tae1^{C110S}, which is modified at a partially buried residue sitting
350 directly behind the catalytic Cys30 site (**Figure 5A**). The Cys110Ser substitution was the top-scoring
351 GOF variant in the D-Met screen and ranked 11th amongst GOF variants in the M9 screen. Using the *E.*
352 *coli* lysis assay, we first confirmed that Tae1^{C110S} indeed lysed cells at a faster rate than Tae1^{WT} in cells
353 grown in both D-Met and M9 minimal media (**Figure 5B**). To rule out indirect effects on toxicity caused
354 by increased protein levels, we assessed Tae1^{C110S} expression by Western blot analysis and did not
355 observe any increase relative to
356 Tae1^{WT} (**Figure 5B**).
357
358 The observation that Tae1 activity
359 could generally be tuned for greater
360 toxicity led us to ask why *tae1* from *P.*
361 *aeruginosa* does not naturally encode
362 Ser110. We considered several
363 explanations, none of which are
364 mutually exclusive. First, it is possible
365 that structural rearrangements
366 introduced by the Cys110Ser
367 substitution may disrupt Tae1
368 interactions with critical molecular
369 partners present in natural T6S-
370 mediated interbacterial interactions but
371 not in our DMS set-up. During T6S
372 competition, Tae1 from *P. aeruginosa*
373 must be delivered to neighboring cells
374 by a complex T6S secretion apparatus
375 that we bypassed with an engineered
376 secretion signal in our screen.
377 Furthermore, Tae1 injected into nearby
378 kin cells is deactivated through binding
379 by a cognate immunity protein, T6S
380 amidase immunity protein 1 (Tai1),
381 preventing lysis. Tai1 is specifically
382 encoded by *P. aeruginosa* and not *E.*
383 *coli*. Second, it is possible that we have
384 not sampled Tae1 fitness across
385 contexts that accurately represent
386 bacterial rivals or competition
387 conditions most relevant for *P.*
388 *aeruginosa* in the wild.
389

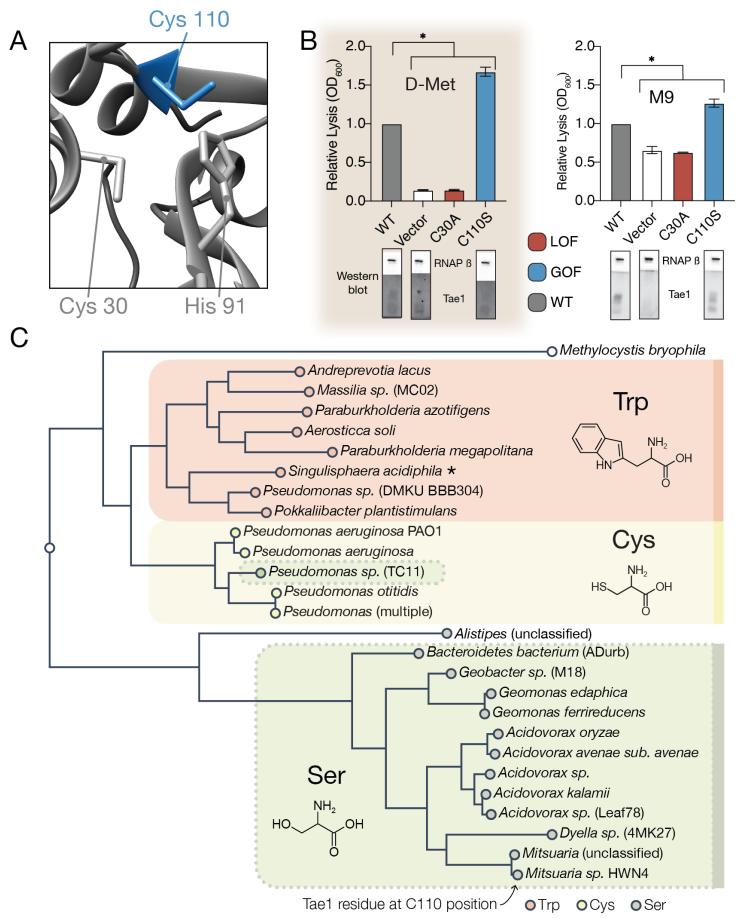

Figure 5. A hyperactive variant of Tae1 is naturally encoded by other *tae* homologs. (A) Ribbon structure diagram at the Tae1 catalytic site. Catalytic dyad residues Cys30 and His91 are indicated along with GOF Cys110. (B) Lysis assays with wild-type Tae1, empty vector and catalytically inactive Tae1^{C30A} as negative controls, and gain-of-function variant Tae1^{C110S} in D-Met and M9 media. Data are means +/- standard deviation, n = 3, * $p < 0.05$. Lysis experiment was repeated 3 independent times, each time with at least.3 technical replicates. Western blots below measure Tae1 protein expression with RNAP as a control. The C110S GOF substitution does is not sensitive to the D-Met induced changes in cell wall architecture. (C) Tae1 family phylogenetic tree. Species with Ser at position 110 are indicted in blue, while those with Cys are in black and those with Trp are in purple. Some but not all Tae1 proteins have evolved to include a Ser at position 110.

390 We therefore investigated whether Ser110 naturally occurs in any Tae1 representatives outside of *P.*
391 *aeruginosa* by searching for family members that encode a serine at residue positions comparable to
392 Cys110, as predicted by structure-based alignments. Surprisingly, we found that approximately half of
393 *tae1*-carrying bacterial species encoded serine residues at the Cys110 position, while some encoded
394 tryptophan (**Figure 5C**). To examine how these three variant classes are taxonomically distributed, we
395 generated a phylogenetic tree of all associated bacterial species and observed correlated divisions
396 across taxonomic clades and the residues at the Cys110 position, with the exception of one
397 *Pseudomonas* species (**Figure 5C**). Considering this observation, we hypothesized that *tae1* evolution
398 may have been locally constrained due to the requirement for Tai1-dependent immunity to prevent self-
399 antagonism.

Hyperactive variant Tae1^{C110S} evades binding and inhibition by cognate immunity

We reasoned that if Tae1 proteins are too structurally divergent, the toxin may evade binding by the cognate Tai1 partner in *P. aeruginosa* (Tai1^{PA}) and consequently antagonize kin cells or other closely related species. To assess whether the Tae1^{C110S} variant affects Tae1–Tai1 interactions, we first assessed whether Tae1^{C110S} adopted any major structural changes by solving its three-dimensional crystal structure (PDB ID: 7TVH) (**Table 2**). We did not observe any major structural rearrangements that would immediately implicate distinct modes of Tai1^{PA}-binding (RMSD=0.746, **Figure 6A**). However, we did observe some key side chain alterations near the Tae1^{C110S} active site, which is the enzyme region most intimately engaged with Tai1^{PA} upon binding (**Supplemental Figure 5**). Most notably, we found that His91 protruded away from the active site of Tae1^{C110S}, which would sterically clash with a loop of Tai1^{PA} that typically inserts into the catalytic cleft (**Figure 6B**). Our structural observations are consistent with the hypothesis that the Cys110 position is important for Tai1 recognition; therefore, serine at this position in *P. aeruginosa* may be disfavored to preserve immunity to the toxin. We generated a tree for the Tai1 protein family, similar to our tree for the Tae1 protein family. Consistent with this possibility, the tree for Tai1 has a similar branching pattern that is coincident with the residue variation at this position (**Supplemental Figure 6**).

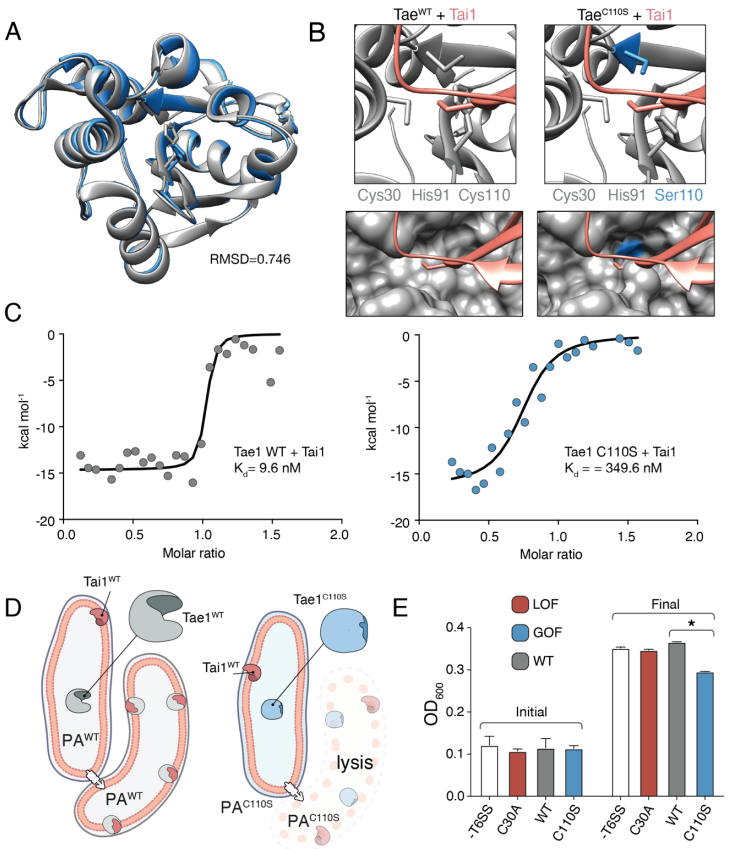

Figure 6. Hyperactive variant Tae1^{C110S} evades binding and inhibition by cognate immunity. (A) Tae1^{WT} ribbon structure diagram (silver) and Tae1^{C110S} ribbon structure diagram (blue) with the His91 side chain shown. C110S mutation does not cause major structural changes, but alters side chains in the active site. (B) Ribbon diagrams of the active sites of Tae1^{WT} (left) and Tae1C110S (right) in complex with Tai1 (pink). Side chains of Cys30, His91, and Cys110 are indicated in gray, and Ser110 in blue. His91 clashes with Tai1 in the active site. (C) Isothermal titration calorimetry determination of binding constants between wild-type Tae1 and Tai1 (left) and Tae1^{C110S} and Tai1 (right). Tae1^{C110S} binds poorly to Tai1. (D) Schematic depicting Tae1 and Tai1 interactions in wild-type *P. aeruginosa* and Tae1^{C110S} *P. aeruginosa.* When wild-type Tae1 is injected into a neighboring cell of the same species, Tai1 binds to it, conferring immunity. Tai1 cannot bind Tae1^{C110S}, thus the mutant Tae1 can cause cell lysis. (E) Fitness assays of *P. aeruginosa* expressing wild-type Tae1 or Tae1^{C110S} from the endogenous locus. *P. aeruginosa* lacking a Type 6 Secretion System (-T6SS) or expressing catalytically inactive Tae1 (C30A) were used as controls. Data are means +/- standard deviation, n = 3, * $p < 0.05$. Competition experiment was repeated 3 independent times, each time with at least.3 technical replicates. Cells expressing Tae1^{C110S} have decreased fitness when compared with wild-type Tae1. See also supplementary figures 6, 7.

We tested our prediction through a series of quantitative *in vitro* Tae1–Tai1 binding experiments. We measured Tai1-binding affinity (Kd) for recombinant Tae1^{WT} and Tae1^{C110S} proteins by isothermal titration calorimetry and found that Tae1^{WT} bound Tai1 with ~36-fold greater affinity than Tae1^{C110S} (9.5 nM Kd and 349.6 nM Kd, respectively) (**Figure 6C**). Toxin–immunity complexes are typically associated with binding affinities in the nM range; thus,

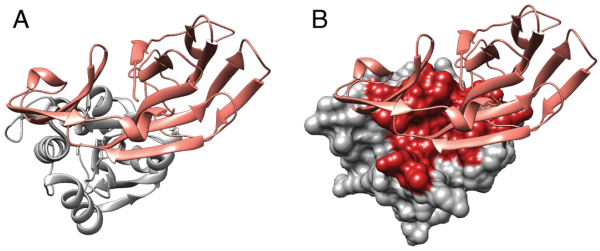

Figure S5. Tae1 – Tai1 interactions. (A) Ribbon diagram of Tae1 (silver) and Tai1 (pink). (B) Tae1 surface diagram, with red residues representing contacts with Tai1. The contacts are based on PDB ID 4EQA.

reduction may preclude the ability of Tai1 to effectively bind its toxin partner *in vivo*. To test whether Tae1^{C110S} evades Tai1-dependent immunity *in vivo*, we constructed a strain of *P. aeruginosa* harboring this mutation (*PA^{C110S}*) with a wild-type strain *(PA^{WT}*). We reasoned that if Tae1^{C110S} escapes Tai1-binding and therefore immune protection, we would observe a decrease in *PA^{C110S}* fitness compared to a wild-type strain (*PA^{WT}*) specifically when grown on solid media which induces T6S (**Figure 6D**). Indeed, for *PA^{C110S}* we observed substantially reduced growth compared to *PA^{WT}* on solid media (**Figure 6E**) but not in liquid media, where T6S is not induced (**Supplemental Figure 7**). This phenotype strongly suggests that Tae1^{C110S} lyses kin cells at a faster rate than Tae1^{WT} can bind and inhibit killing, leading to a fitness cost for this strain.

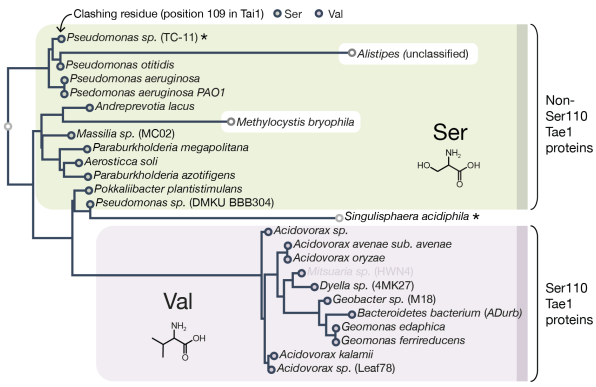

Figure S6. Tai1 family phylogenetic tree. The residue at position 109 is either a Val (in Tai1s corresponding to Tae1_S110 proteins) or a Ser (in Tai1s corresponding to Tae1 non-S110 proteins). The tree contains the same species found in the Tae1 tree, except for *Mitsuaria* (unclassified) and *Pseudomonas* (multiple). Coloring of the species also matches that in the Tae1 tree. The sequences in the tree were identified using a published heuristic approach that specifically searches for T6S effector toxins. ML tree was inferred using PhyML v20160115 ran with model JTT and parameters: --alpha e -o tlr --bootstrap -2 -f m --nclasses 4 --pinv e. Branch supports are the Chi2-based parametric values returned by the approximate likelihood ratio test. Major clades had 90 or higher support values. The species marked with an asterisk have a Ser at position 110 in the corresponding Tae1 protein (for *Pseudomonas* sp. TC-11) or have an Ala at position 109 for the Tai1 protein (for *Singulisphaera acidiphila*).

Together, our *in vitro* and *in vivo* results suggest that the fitness cost of evading Tai1-binding likely limits the proliferation of Tae1^{C110S} in the wild. This interaction presents an evolutionary bottleneck that impedes certain toxin variants, such as Tae1^{C110S}, from broadly taking hold across all species. More generally, our DMS screening approach allowed us to systematically probe function across different *in vivo* contexts, identifying two distinct but important selective pressures – substrate-specificity and toxin–immunity interactions – that may, in combination, shape diversity across the Tae1 toxin superfamily.

DISCUSSION

The Tae superfamily of interbacterial toxins is phylogenetically, structurally, and functionally diverse[7,10]. Here, we show that sequence-based differences in *tae* homologs shape Tae proteins and their complex substrate, the PG that constitutes the bacterial cell wall. Our studies revealed that Tae1 engages PG through a circumferential interface that is more extensive than most proteases or other enzymes. This unexpectedly large interaction surface may be key for dictating species-specific toxicity of Tae proteins and consequently serve as a major driver of Tae superfamily diversification. This surface could also mediate processivity across PG. Taes have many other binding partners as well. These toxins interact with the T6SS apparatus for secretion, which likely limits effector size to a single, minimal catalytic unit[4,26]. Therefore, unlike other larger multi-domain housekeeping PG hydrolases[27], Tae toxins rely on a relatively restricted set of surfaces to mediate many distinct, functional interactions. Our unbiased, high throughput DMS analyses revealed that determinants for Tae1 cell wall-binding and immunity-binding partially overlap. Our findings suggest that accommodation of multiple, distinct functions likely constrains evolution of Tae enzymes in nature despite intrinsic potential for enhanced toxicity. Extensive Tae functional surfaces may also point to the existence of additional unknown interaction partners within bacteria. This principle may prove true for other T6S

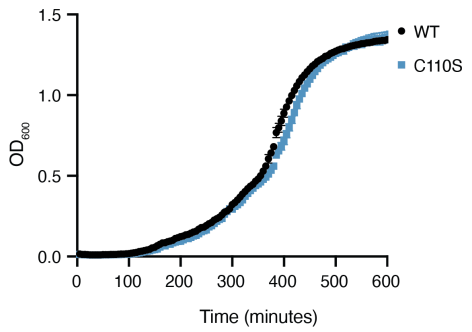

Figure S7. Competition assay in liquid culture. Growth in *P. aeruginosa* expressing wild-type Tae1 or Tae1^{C110S} from the endogenous locus in liquid culture. Data are means +/- standard deviation, n = 3. Growth experiment was repeated 3 independent times, each time with at least.3 technical replicates.

toxins and proteins; comprehensive mapping of functional determinants by DMS may power further functional discovery.

Complementing traditional biophysical approaches with DMS allowed us to probe molecular interactions in physiological states that are difficult to capture *in vitro*. Our current understanding of enzyme interactions with the bacterial cell wall draws mostly from biochemical analyses conducted in solution, posing a fundamental challenge for proteins with three-dimensional highly-crosslinked macromolecular substrates. Considering the architectural complexity of the bacterial cell wall, a large ring-like surface looping around Tae1 seems critical for toxicity *in vivo*. This observation could be due to at least two possible modes of binding that we posit may be unique to enzymes with macromolecular substrates. First, we theorize that a more extensive, non-linear substrate binding domain may enable an enzyme to specifically recognize a particular conformational state. Three-dimensional configurations of the cell wall may be an important feature for a toxin like Tae1 to detect, given that this could affect protein localization to specific cell wall features that have distinct shapes. It has been previously observed that a critical hole size in the cell wall is necessary for bacterial lysis[28]; thus localized action of PG enzymes may provide an important advantage for Tae toxins. Another potential advantage of binding a specific substrate configuration is that this would enable a Tae enzyme to distinguish between different species or incorporation states of PG fragments. Indeed, certain endogenous enzymes, such as FtsN interact exclusively with complex PG chains of a certain length[29].

Another possibility is that the large functional surface comprises several different PG-binding domains that streamline substrate recognition or underlie enzyme processivity. This has been suggested for a cell wall digesting enzyme, Lysostaphin from *Staphylococcus*, which exhibits two large PG-binding surfaces on opposite sides of the enzyme[23]. Multi-step binding would support the “smart autolysins” model postulated by Arthur Koch[30]. This model hints at the ability of hydrolase enzymes to recognize “stretched” areas of PG. The resulting advantage for hydrolytic cell wall enzymes is that this type of recognition decreases substrate search dimensionality from random 3-D diffusion to facilitated diffusion by searching along the PG sacculus one plane at a time[31]. This may be particularly important for rapid, effective recognition of substrates within a large cage-like 3D target like the cell wall, which is key for potent, fast-acting toxins. This mechanism is also commonly adopted by DNA-binding proteins, which dock nonspecifically to DNA before searching for specific cut sites[32,33]. Multi-step binding may also lead to processive activity along PG by ensuring that Tae enzymes remain tethered to the cell wall substrate after each hydrolysis event, which would allow for “stepwise chewing.” This would be yet another mechanism to increase the odds of localized, lytic activity.

In total, our combined use of biophysical and high throughput genetic approaches uncovered novel insights into Tae toxin activity inside bacterial cells, providing a window into how small, single-domain enzymes carry out several, distinct functions *in vivo*. Our leveraging of a multi-pronged strategy was critical for overcoming technical obstacles inherent to proteins that interact with complex, insoluble molecules, providing access to a class of macromolecular interactions that are not well understood. The biophysical and kinetic parameters of proteins with three-dimensional highly-crosslinked macromolecular substrates[34,35] are dissimilar from those well-established for small, soluble substrates, and future adoption of combinatorial approaches such as ours may improve our understanding of general binding principles across these important enzymes that are ubiquitous across life. Additionally, the ability to quickly generate rich quantitative heatmaps for enzymes across different experimental conditions enables more sophisticated computational analyses. Predictive representation learning of unbiased, functional datasets across multiple biological conditions could help us anticipate *a priori* the functional consequences of sequence-based phylogenetic diversity. A deeper understanding of functional design principles would also enable more effective leveraging of evolutionary innovations to engineer new molecules tailored to physiological contexts with important, useful applications.

ACKNOWLEDGEMENTS

We would like to thank Dr Doug Fowler (University of Washington) and Dr Eric Chow (University of California – San Francisco) for their help with setting up the deep mutational scanning pipeline. We are also grateful to Dr David Mavor (University of Massachusetts Chan Medical School), Dr Robert Newberry (University of Texas – Austin), Dr Martin Kampmann (University of California – San Francisco), and Dr James Fraser (University of California – San Francisco) for their assistance with sequencing data analysis. We say thanks to Dr Kari Herrington and Dr SoYeon Kim (University of California – San Francisco) for their contribution with microscopy data collection and analysis. We also thank Dr George Meigs and Dr James Holton (Lawrence Berkeley National Lab), and Dr Michael Thompson (University of California – Merced), for their help with x-ray crystallography data collection and analysis. We are grateful to Dr Mark Kelly for his help with setting up NMR data collection (University of California – San Francisco). We also thank to Dr Parnian Lak (University of California – San Francisco) for her help with setting up the ITC experiments. Lastly, we greatly appreciate the input regarding the experiments and the manuscript from members of the Chou lab at the University of California – San Francisco (Kristine Trotta, Calla Martyn, Fauna Yarza, Elizabeth A. Martinez-Bond, Patrick Grimes, Dr Domokos Lauko). Anne Sapiro received a Life Sciences Research Foundation fellowship from the SVCF-Wave Fund. Financial support from the IR-RMN-THC FR3050 CNRS for conducting the research on the 950 MHz NMR spectrometer is gratefully acknowledged. We would also like to thank the Chan Zuckerberg Biohub as well as the Sanghvi-Agarwal Innovation Award for their financial support.

COMPETING INTERESTS

The authors declare no competing interests.

METHODS

Docking analysis

Modeling was conducted with SwissDock using the default parameters[36]. The Tae1 monomer with PDB ID: 4EOB was used here[10]. The crosslinked PG dimer was constructed with MarvinSketch, based on ChEBI:61388. This viable pose was chosen based on the proximity of the active site nucleophile Cys30 to the scissile bond within the PG substrate.

Preparation of long chains of PG

PG isolation and HPLC analysis were conducted according to an established protocol[37] with the following modifications. Briefly, *E. coli* BW25113 cells were grown in 200ml LB media to mid-log phase. The cells were harvested by centrifugation at 5000 x g for 15min, after which they were suspended in 300μl of fresh LB media and added to 600μl 6% SDS solution in a 2ml Eppendorf tube. The cells were boiled for 3hrs in a heat block and then maintained in the SDS solution at 4°C until needed. The boiled sacculi were washed 5 times with MQ water to remove the SDS. Each wash consisted of 15min centrifugation at 21000 x g followed by decanting of the supernatant and resuspending in 1ml of MQ water by vortexing. After the final wash, the sacculi were suspended in Pronase E digestion buffer (10mM Tris-HCl pH 7.2 and 0.06% NaCl) and were treated for 2hrs at 60°C with activated Pronase E (100μg/ml final concentration, pre-treated for 2hrs at 60°C in the digestion buffer; supplier: VWR). The sacculi were incubated at 100°C for 10min to inactivate the Pronase E and were washed 3 times with 1ml of MQ water, with vortexing to resuspend. The sacculi were treated with purified Tae3 enzyme (10μM) overnight at 37°C in 20mM HEPES pH7.0 and 100mM NaCl buffer. The PG fragments were finally dialyzed using 500Da molecular weight cutoff tubing (Biotech CE Tubing, Spectra/Por) and dried on a Vacufuge concentrator to remove all liquid. They were stored at -80°C and were redissolved

before each NMR experiment with minimal volume to yield the desired enzyme to substrate concentrations.

NMR experiments

NMR experiments for backbone assignments were performed at 25°C on a Bruker 950 MHz AVANCE (Institut de Biologie Structurale in Grenoble) or Varian INOVA spectrometers (600 and 800 MHz instruments at Pacific Northwest National Laboratories). NMR samples for determination of Tae1 resonance assignments consisted of 0.3 to 0.6 mM [^{13}C,^{15}N]-Tae1 in citrate buffer pH 5.5 with 150 mM NaCl, 100 μM EDTA containing 5% D_2O. Assignment of backbone resonances was accomplished by analysis of standard triple-resonance experiments (^{1}H,^{15}N)-HSQC, HNCA, HNCOCA, HNCACB, CBCA(CO)NH, and HNCO spectra[21]). Assignments of Tae1 resonances in 20mM HEPES or NaP_i ,150 mM NaCl, 100 μM EDTA at pH 7.0 were determined by collecting a series of [^{1}H,^{15}N]-HSQC spectra titrating the sample from pH 5.5 to 7.0. These assignments were confirmed by collecting an HNCO spectrum under the final conditions at pH 7.0. NMR data were processed and analyzed using NMRPipe[38] and NMRView[39,40] (for the residue assignments, see **Supplemental Figure 8**). See **Supplemental Table 2** for the peak values and **Supplemental Table 3** for CSP (Δδ) values.

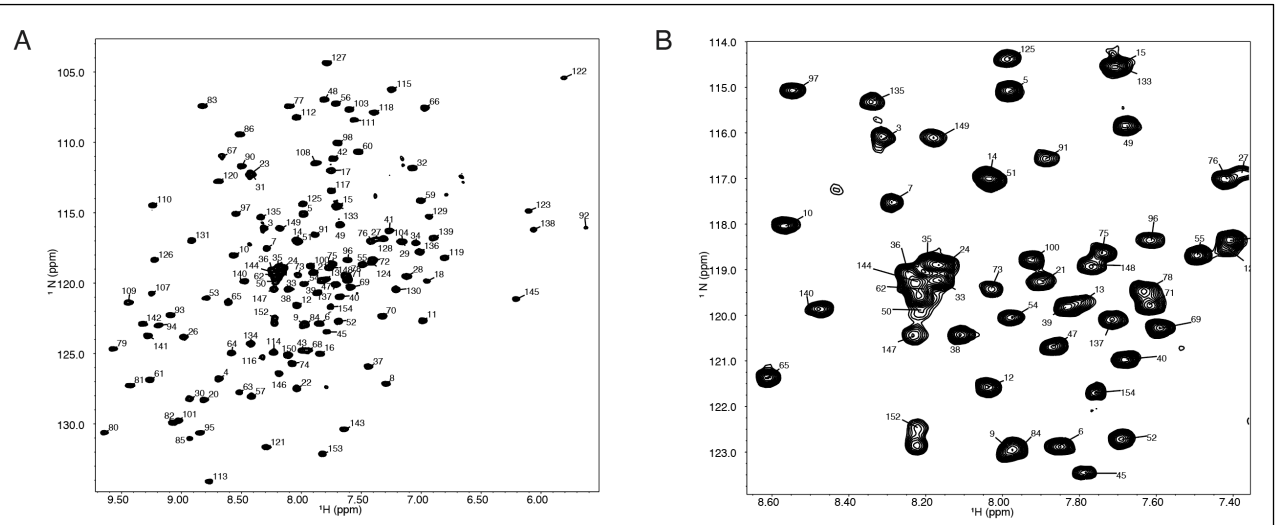

Figure S8. (^{1}H,^{15}N)-TROSY spectrum of 150mM Tae1 in 20mM HEPES, 100mM NaCl, pH 7.0 showing resonance assignments for backbone amides. B) Expanded view of a smaller region of the same spectrum.

All titration experiments were conducted at the Institut de Biologie Structurale in Grenoble or at the UCSF NMR facility in Genentech Hall (San Francisco). PG ligand was dialyzed against water using a float dialysis membrane device with a 100-500 Da cut-off (Spectrum Laboratories, Inc) and lyophilized before preparation of a concentrated stock solution in NMR buffer. Before aliquoting the samples or before lyophilization, the concentration of the stock solution was estimated by liquid-state NMR using the Eretic pulse sequence[41] and a reference 1 mM sucrose sample in 90%:10% H_2O:D_2O. Interaction studies with ^{15}N-labelled Tae1 and PG substrates were monitored by superimposition of ^{15}N-BEST-TROSY spectra at 25°C for different substrate-to-protein ratio[42]. A 50μM ^{15}N labeled Tae1_C30A was titrated with 500 and 1000 μM of purified muropeptide. CcpNmr2.4 was used to monitor protein CSP for every assigned amide resonance by superimposition of the ^{15}N-BEST-TROSY spectra. CSPs (Δδ) were calculated on a per-residue basis for the highest substrate-to-protein ratio.

E. coli lysis assays

The pBAD vector was used to clone Tae1 variants of interest[43]. The Tae1 wild-type was initially amplified from a previously published pET22::Tae1 construct[10], together with the pelB signal sequence. All variants were constructed based on this pelB_pBAD::Tae1 template. See **Table 1** for all the primers

636 used to clone Tae1 and the different variants. SOE-PCR was used to introduce the individual
637 mutations, followed by restriction enzyme digestion and ligation. pBAD::Tae1 constructs were always
638 transformed freshly into *E. coli* BW25113 chemically competent cells and a LB culture with antibiotic
639 was immediately started after the transformation outgrowth period. The culture was diluted 1 to 100 on
640 the following day into LB media in the presence of antibiotic selection. After reaching OD_{600} of 0.2,
641 protein expression was induced with 0.25% arabinose and cell lysis was monitored overnight on a
642 Biotek plate reader.
643
644 DMS library construction and assay
645 pET22b vector was chosen for library construction. This vector contains the pelB signal sequence that
646 would allow the expression of Tae1 variants in the cell periplasm. The preparation of variants was
647 achieved through an error-prone PCR mutagenesis kit (GeneMorph II Random Mutagenesis Kit –
648 Agilent Technologies), following the manufacturer's instructions in order to insure high proportion of
649 single-mutant variants. The variants were cloned via restriction enzyme cloning. In order to track the
650 behavior of variants, each one was barcoded with a unique DNA sequence. The barcodes were
651 introduced immediately after the Tae1 coding sequence via Gibson assembly cloning (In-Fusion HD
652 Cloning Kit – Takara Bio). Our Next-Generation sequencing strategy comprised two stages. First, the
653 entire library was sequenced to determine the barcode corresponding to each variant. This was
654 accomplished using 300bp forward and reverse reads on the MiSeq Illumina platform (MiSeq Reagent
655 Kit v3). Using this information, a dictionary was prepared to demonstrate the relationships between
656 variants and barcodes. The dictionary was prepared by following previously published scripts[44] with
657 some modification (see the GitHub directory "ChouLab dictionary" for the steps and scripts). For each
658 of the subsequent DMS experiments, 25bp reads on a NextSeq Illumina platform (conducted at Chan
659 Zuckerberg BioHub) were used to sequence only the barcode region. For data analysis and DMS
660 scores calculations, we used Enrich2 software[17]. The barcode dictionary was used to convert barcodes
661 to variants. Please see the "Choulab DMS data analysis" GitHub directory for detailed information on
662 data analysis in Enrich2. For the DMS experiments in this study, the DMS library was grown for 3hrs at
663 37°C in M9 minimal medium (or M9 supplemented with 20mM D-Methionine) before distributing across
664 a 96-well plate. A set of 24 wells was combined for each experimental time point in order to obtain
665 enough DNA for library amplification. Libraries were amplified for 9 cycles using Phusion high-fidelity
666 polymerase to minimize any masking of differences in abundance. The libraries were gel purified,
667 quantified using Qubit, and their concentrations were adjusted according to Illumina instructions before
668 sequencing. The 0hrs time point (DMS library before any growth) was chosen as the input of the 96-
669 well plate incubation. After growth to OD_{600} 0.2, protein expression was induced with 1mM IPTG. Cells
670 were collected 2hrs after induction that would serve as the output time point. All of the scripts used in
671 the paper are available on GitHub at https://github.com/AtanasDRadkov/ChouLab_DMS. The data files
672 are available on NCBI, Sequence Read Archive – PRJNA803461.
673
674 Clustering analysis
675 K-means clustering analysis was conducted using previously published scripts[18] to group Tae1
676 positions into categories based on their fitness scores. We calculated spatial clusters by 1) sorting the
677 fitness score vectors for each position 2) trimming the vectors to match vector lengths (discarding no-
678 data values) 3) calculating a difference by subtracting the two sorted and trimmed vectors, and 4)
679 calculating the distance – mean of the absolute value of the vector difference. The distance between a
680 candidate position and a cluster of positions is calculated as the average of the distance between the
681 candidate position and the three closest non-self positions in the cluster. Clustering was performed over
682 10 rounds following the initial seeded round, and convergence was confirmed by observing that five
683 repetitions gave identical clusters. The results yielded five clusters, including a loss-of-function
684 phenotype cluster which was the focus of the study. The same analysis was performed for both DMS
685 experiments. See the GitHub directory "ChouLab clustering" for the steps and scripts. All of the scripts
686 used in the paper are available on GitHub at https://github.com/AtanasDRadkov/ChouLab_DMS.

687
688 HPLC PG analysis
689 PG isolation and HPLC analysis were conducted as described[37] with the following modifications. Briefly,
690 *E. coli* BW25113 cells were grown in 200ml LB (or LB plus 20mM D-Met) to mid-log phase. The cells
691 were harvested by centrifugation at 5000 x g for 15min, after which they were suspended in 300μl fresh
692 LB and added to 600μl of 6% SDS solution in a 2ml Eppendorf tube. The cells were boiled for 3hrs in a
693 heat block and then maintained in the SDS solution at 4°C until needed. Before any treatments, the
694 boiled sacculi were washed 5 times with MQ water to remove the SDS. Each wash consisted of 15min
695 centrifugation at 21000 x g followed by decanting of the supernatant and resuspending in 1ml MQ water
696 by vortexing. After the final wash, the sacculi were suspended in Pronase E digestion buffer (10mM
697 Tris-HCl pH 7.2 and 0.06% NaCl) and were treated for 2hrs at 60°C with Pronase E (100μg/ml final
698 concentration, pre-treated for 2hrs at 60C in the digestion buffer; supplier: VWR). The sacculi were
699 incubated at 100°C for 10min to inactivate the Pronase E. Enzymatic treatments with Tae1 variant
700 enzymes were conducted at this point using 20mM HEPES pH7.0, 100mM NaCl buffer. Tae1 enzyme
701 was added to 1μM final concentration and the reactions were incubated at room temperature for 10min,
702 followed by 10min at 100°C to inactivate the enzyme. The sacculi were washed 3 times as described
703 above. Finally the sacculi were solubilized using 25μg/ml final concentration of mutanolysin (Sigma-
704 Aldrich) in 10mM Tris-HCl pH 7.2 and 0.06% NaCl after overnight digestion in a 37°C shaker. To
705 prepare PG fragments for HPLC analysis, the mutanolysin treatment was incubated at 100°C for 10min,
706 followed by centrifugation to remove any debris, alkalinization with 0.5M borate buffer and reduction
707 with sodium borohydride for 1hr at room temperature. The reduced PG fragments were acidified to pH
708 3-4 with 50% o-phosphoric acid and filtered (PVDF syringe filters, 0.22μm, 0.4mm - Tisch Scientific)
709 before the HPLC injection. The HPLC instrument, method, and buffers were the same as described
710 previously[45].
711
712 Protein purification
713 All Tae proteins, and Tai1 protein, used in this study were purified according to an established
714 protocol[10] using pET29b+ vector and 3hrs induction in a 37°C shaker with 1mM IPTG. Buffers for metal
715 affinity chromatography were 20mM HEPES pH7, 100mM NaCl, 20mM imidazole and 20mM HEPES
716 pH7, 100mM NaCl, 400mM imidazole. Buffer for size exclusion chromatography (SEC) was 20mM
717 HEPES pH7, 100mM NaCl. The SEC was performed using an isocratic gradient on an AKTA pure
718 instrument with a HiPrep 16/60 Sephacryl S-200 HR column. For isotopically labeled Tae1_C30A, the
719 same plasmid constructs were used, but the expression was conducted in M9 minimal medium
720 prepared with ^{15}N-ammonium chloride (5g per liter media) (M9 minimal medium prepared according to
721 Cold Spring Harbor Protocols). The cells were grown and induced as described above. The same
722 purification procedure was used as described above.
723
724 Tae1 phylogenetic tree
725 Initial candidates of the Tae1 family as identified in Russell et al.[7] were aligned and used as a seed in a
726 PSI-BLAST search. Significant results were downloaded and aligned using MAFFT. Candidates
727 containing the critical Cys-His dyad were kept, and other candidates discarded. Final candidates were
728 re-aligned. Default parameters were used for all steps. Multisequence alignment (ClustalW algorithm)
729 and phylogenetic trees (PhyML analysis) were prepared on GenomeNet (at www.genome.jp).
730
731 *P. aeruginosa* strain construction
732 *P. aeruginosa* strains used in this study were derived from the sequenced strain PAO1[46]. *E. coli* strain
733 SM10 was used for conjugal transfer of pEXg2 plasmids for homologous recombination as described
734 previously[5]. All deletions were in-frame and were generated by exchange with deletion alleles
735 constructed by SOE PCR, followed by restriction enzyme cloning into pEXg2 vector. See **Table 1** for
736 the primers used to delete genes *pppA* and *retS*, and to introduce the C110S mutation into *tae1*.
737

Contact-dependent fitness assays

Fitness assays were performed with overnight *P. aeruginosa* cultures. The assays were performed on solid media (LB without added NaCl containing 3% agar) using nitrocellulose membranes (Amersham Biosciences Hybond-N+, 0.45um) to insure close contact between the cells[5]. The OD_{600} was adjusted to 1.0 for all strains. 10μl were spotted onto a membrane to initiate the contact-dependent fitness assays. The assays were incubated for 6 hrs at 37°C after which the spots were removed with a razor blade, placed in a tube with glass beads, shaken on a bead beater (BeadBug microtube homogenizer; Z763705, Sigma) for 20sec at 4000rpm, and the suspended cells were distributed across a 96-well plate (3 x 200μl wells for each competition tube) for OD_{600} measurements on a Biotek plate reader.

Isothermal titration calorimetry

Isothermal titration calorimetry experiments were performed at 298°K using a Microcal ITC200 (GE Healthcare, Northampton, MA). Stock solutions of Tae1 and Tai1 were dialyzed overnight at 277°K in the same buffer (50mM NaCl, 20mM Tris 7.0). The cell was filled with 200μL of Tai1 protein at a concentration of 20μM to which 150μM of Tae1 protein was titrated. For 25 titrations of 1.5μL of Tae1 into Tai1 the heat of binding was recorded. Data were extracted and fitted using the single-site binding model following manufacturer's instructions.

$Tae1^{C110S}$ crystal structure

$Tae1^{C110S}$ protein crystals were generated by hanging drop vapor diffusion at 25°C from a 1:1 mixture of 10 mg/ml protein (in 20mM HEPES pH7, 100mM NaCl, 5% glycerol) with 0.2 M sodium thiocyanate, 0.1 M HEPES pH 7.5, 20% PEG3350 for 24hrs (same conditions that were used for initial structure of Tae1[10]). Crystals were directly used for diffraction data collection at the Lawrence Berkeley National Laboratory Advanced Light Source Beamline 8.3.1[47]. Coot[48] and Maximum-Likelihood[49] refinement with PHENIX were used for iterative building and refinement. Structure was validated by MOLProbity[50] and visualized with Chimera[51]. Coordinates and structure factors were deposited in the Protein Data Bank (PDB ID: 7TVH).

789 **Tables**

790

791 **Table1.** Primers used in this study

Name	Sequence
pET22_Tae1_C110S_F1	CCGATGTGCTGGTCCGGCAGCATCGCCGGC
pET22_Tae1_C110S_F2	GGTGGTGGTGCTCGAG
pET22_Tae1_C110S_R1	GCCGGCGATGCTGCCGGACCAGCACATCGG
pET22_Tae1_C110S_R2	TGGATATCGGAATTAATTCGGATC
pET29_Tae1_C110S_F1	CCGATGTGCTGGTCCGGCAGCATCGCCGGC
pET29_Tae1_C110S_F2	GGTGGTGGTGCTCGAG
pET29_Tae1_C110S_R1	GCCGGCGATGCTGCCGGACCAGCACATCGG
pET29_Tae1_C110S_R2	GGGAATTCCATATGGACAGTCTCGATCAATGC
pBAD_Tae1_F	TAGTACAGAGAATTCACCATGAAATACCTGCTGCCGACCGCTGCTGC
pBAD_Tae1_R	TCAATCAGTATCTAGATTACTCGAGACTGGCCCTGGGCAGGCTG
pEXG2_pppA_F1	TGTTAAGCTAAAGCTTGTCGGTCGCTATTTCCCGCTGAC
pEXG2_pppA_F2	GCATACCCGGTTAAGGACAACTGATGGTGAACTCGAGCCGCAAGCATGCTGAA
pEXG2_pppA_R1	TCAATCAGTATCTAGAGCCGGTGAGGATCTCGTAGAGCAC
pEXG2_pppA_R2	CCGGAAGTTCTATGTCCATGTCCGTCTCAGAATTCAGCATGCTTGCGGCTCGAGTT
pEXG2_retS_F1	TCAATCAGTATCTAGACGGAAACCCAGCCGATCATGG
pEXG2_retS_F2	AACTCGAGCCGCAAGCATGCTGAAGGCGAAGTCCCTTCGAAGGTG
pEXG2_retS_R1	TGTTAAGCTAAAGCTTCCAGCATCTTCAGGTAGACGC
pEXG2_retS_R2	TTCAGCATGCTTGCGGCTCGAGTTGCCTACTGGGTCGGCGAACGC
pEXG2_Tae1C110S_F1	TCAAGTACTAGAGCTCGTGGTGCACCGCGAGGACATCTC
pEXG2_Tae1C110S_F2	CTGCCACTCCAGCACATCGGGTAC
pEXG2_Tae1C110S_R1	TATCAGAAACCTGCAGGTAGGCCAGCGACTGCATGCCGTAG
pEXG2_Tae1C110S_R2	GATGTGCTGGAGTGGCAGCATCGCC
pBAD_Tae1L21S_F	AGCTGGGACAAGAGCTACAGCGCCGGCACCCCG
pBAD_Tae1L21S_R	CTTGTTCGGGGTGCCGGCGCTGTAGCTCTTGTC
pBAD_Tae1G48S_F	GGCGTACCGATGCCCCGCAGCAACGCCAACGCC
pBAD_Tae1G48S_R	GACCATGGCGTTGGCGTTGCTGCGGGGCATCGG
pBAD_Tae1G56S_F	GCCAACGCCATGGTCGACAGCCTGGAGCAGAGC
pBAD_Tae1G56S_R	GGTCCAGCTCTGCTCCAGGCTGTCGACCATGGC
pBAD_Tae1G42S_F	TCGGTGGCCGCCGAGCTGAGCGTACCGATGCCC
pBAD_Tae1G42S_R	GCCGCGGGGCATCGGTACGCTCAGCTCGGCGGC
pBAD_Tae1V43S_F	GTGGCCGCCGAGCTGGGCAGCCCGATGCCCCGC
pBAD_Tae1V43S_R	GTTGCCGCGGGGCATCGGGCTGCCCAGCTCGGC
pBAD_Tae1A52P_F	CCCCGCGGCAACGCCAACCCGATGGTCGACGGC
pBAD_Tae1A52P_R	CTCCAGGCCGTCGACCATCGGGTTGGCGTTGCC
pBAD_Tae1S144A_F	CTCAACTACTACGTCTACGCCCTGGCCAGTTGC
pBAD_Tae1S144A_R	CAGGCTGCAACTGGCCAGGGCGTAGACGTAGTA
pBAD_Tae1S147A_F	TACGTCTACTCCCTGGCCGCCTGCAGCCTGCCC
pBAD_Tae1S147A_R	GGCCCTGGGCAGGCTGCAGGCGGCCAGGGAGTA
pBAD_Tae1S149A_F	TACTCCCTGGCCAGTTGCGCCCTGCCCAGGGCC
pBAD_Tae1S149A_R	GAGACTGGCCCTGGGCAGGGCGCAACTGGCCAG
pBAD_Tae1A116T_F	TGCGGCAGCATCGCCGGCACTGTCGGCCAGAGC
pBAD_Tae1A116T_R	GCCCTGGCTCTGGCCGACAGTGCCGGCGATGCT
pBAD_Tae1D134N_F	CAGGTGTGGAATCGCACCAACCGCGACCGCCTC
pBAD_Tae1D134N_R	GTAGTTGAGGCGGTCGCGGTTGGTGCGATTCCA
pBAD_Tae1S147I_F	TACGTCTACTCCCTGGCCATTTGCAGCCTGCCC
pBAD_Tae1S147I_R	GGCCCTGGGCAGGCTGCAAATGGCCAGGGAGTA
DMS_Lib_Amplify_F	AATGATACGGCGACCACCGAGATCTACACCTTTCGGGCTTTGTTAGCAG
DMS_Lib_Amplify_R1	CAAGCAGAAGACGGCATACGAGATGGAACGGAGTGACTGGAGTTCAGACGTGTGC TCTTCCGATCTTCGATAGTAGCCTATGAAGCATGCTTACTA

DMS_Lib_Amplify_R2	CAAGCAGAAGACGGCATACGAGATCGGCACATGTGACTGGAGTTCAGACGTGTGC TCTTCCGATCTTCGATAGTAGCCTATGAAGCATGCTTACTA
DMS_Lib_Amplify_R3	CAAGCAGAAGACGGCATACGAGATTACCCTTGGTGACTGGAGTTCAGACGTGTGC TCTTCCGATCTTCGATAGTAGCCTATGAAGCATGCTTACTA
DMS_Lib_Amplify_R4	CAAGCAGAAGACGGCATACGAGATTAGGTGTCGTGACTGGAGTTCAGACGTGTGC TCTTCCGATCTTCGATAGTAGCCTATGAAGCATGCTTACTA
DMS_Lib_Amplify_R5	CAAGCAGAAGACGGCATACGAGATGAATCACTGTGACTGGAGTTCAGACGTGTGC TCTTCCGATCTTCGATAGTAGCCTATGAAGCATGCTTACTA
DMS_Lib_Amplify_R6	CAAGCAGAAGACGGCATACGAGATCATAGAGTGTGACTGGAGTTCAGACGTGTGC TCTTCCGATCTTCGATAGTAGCCTATGAAGCATGCTTACTA
DMS_custom_seq_F	GGTGGTGCTCGACGATAGCACGTCTCTGACACCGAATTC
DMS_custom_seq_R	GCCCAGCCGGCGATGGCCATGGATATCGGAATTAATTC

829 **Table2.** X-ray data collection and refinement statistics for Tae1^{C110S} (PDB ID: 7TVH)
830

	Crystal 1	831
Data collection		
Space group	P 1 21 1	
Cell dimensions		
a, *b*, *c* (Å)	39.121 108.512 82.402	
Resolution (Å)	65.56 - 1.71 (1.77 - 1.71)	
R_{sym} or R_{merge}	0.03896 (0.9019)	
I / *I*	10.48 (0.80)	
Completeness (%)	98.45 (87.02)	
Redundancy	2.00 (2.00)	
$CC_{1/2}$	0.999 (0.469)	
Refinement		
Resolution (Å)	65.56 - 1.71	
No. reflections	72921 (6436)	
R_{work} / R_{free}	0.2113 / 0.2430	
No. atoms	4673	
Protein	4277	
Water	396	
B-factors		
Protein	38.21	
Water	43.00	
R.m.s. deviations		
Bond lengths (Å)	0.006	
Bond angles	0.77	
Ramachandran favored (%)	98.09	
Ramachandran allowed (%)	1.91	
Ramachandran outliers (%)	0	
Rotamer outliers	0	

832 *Values in parentheses are for highest-resolution shell.
833
834
835
836
837
838
839
840
841
842
843
844
845
846
847
848
849
850

851 **References:**
852

853 1. Peterson, S. B., Bertolli, S. K. & Mougous, J. D. The central role of interbacterial antagonism in
854 bacterial life. *Current Biology* **30**, R1203–R1214 (2020).
855 2. Jani, A. J. & Cotter, P. A. Type VI Secretion: Not just for pathogenesis anymore. *Cell Host &*
856 *Microbe* **8**, 2–6 (2010).
857 3. Schwarz, S., Hood, R. D. & Mougous, J. D. What is type VI secretion doing in all those bugs?
858 *Trends in Microbiology* **18**, 531–537 (2010).
859 4. Russell, A. B., Peterson, S. B. & Mougous, J. D. Type VI secretion system effectors: poisons with a
860 purpose. *Nat Rev Microbiol* **12**, 137–148 (2014).
861 5. Russell, A. B. *et al.* Type VI secretion delivers bacteriolytic effectors to target cells. *Nature* **475**,
862 343–347 (2011).
863 6. Hood, R. D. *et al.* A Type VI Secretion System of *Pseudomonas aeruginosa* targets a toxin to
864 bacteria. *Cell Host & Microbe* **7**, 25–37 (2010).
865 7. Russell, A. B. *et al.* A widespread bacterial Type VI Secretion effector superfamily identified using a
866 heuristic approach. *Cell Host & Microbe* **11**, 538–549 (2012).
867 8. Russell, A. B. *et al.* A Type VI Secretion-related pathway in Bacteroidetes mediates interbacterial
868 antagonism. *Cell Host & Microbe* **16**, 227–236 (2014).
869 9. LaCourse, K. D. Conditional toxicity and synergy drive diversity among antibacterial effectors.
870 *Nature Microbiology* **3**, 9 (2018).
871 10. Chou, S. *et al.* Structure of a peptidoglycan amidase effector targeted to Gram-negative bacteria by
872 the Type VI Secretion System. *Cell Reports* **1**, 656–664 (2012).
873 11. Vollmer, W., Blanot, D. & De Pedro, M. A. Peptidoglycan structure and architecture. *FEMS*
874 *Microbiol Rev* **32**, 149–167 (2008).
875 12. Vollmer, W. & Seligman, S. J. Architecture of peptidoglycan: more data and more models. *Trends in*
876 *Microbiology* **18**, 59–66 (2010).

877 13. Furchtgott, L., Wingreen, N. S. & Huang, K. C. Mechanisms for maintaining cell shape in rod-
878 shaped Gram-negative bacteria: Rod-shape maintenance in Gram-negative bacteria. *Molecular*
879 *Microbiology* **81**, 340–353 (2011).
880 14. Elazar, A. *et al.* Mutational scanning reveals the determinants of protein insertion and association
881 energetics in the plasma membrane. *eLife* **5**, e12125 (2016).
882 15. Barad, B. A. *et al.* Differences in the chitinolytic activity of mammalian chitinases on soluble and
883 insoluble substrates. *Protein Science* **29**, 952–963 (2020).
884 16. Fowler, D. M. & Fields, S. Deep mutational scanning: a new style of protein science. *Nat Methods*
885 **11**, 801–807 (2014).
886 17. Rubin, A. F. *et al.* A statistical framework for analyzing deep mutational scanning data. *Genome*
887 *Biol* **18**, 150 (2017).
888 18. Thompson, S., Zhang, Y., Ingle, C., Reynolds, K. A. & Kortemme, T. Altered expression of a quality
889 control protease in *E. coli* reshapes the in vivo mutational landscape of a model enzyme. *eLife* **9**,
890 e53476 (2020).
891 19. Schanda, P. *et al.* Atomic model of a cell-wall cross-linking enzyme in complex with an intact
892 bacterial peptidoglycan. *J. Am. Chem. Soc.* **136**, 17852–17860 (2014).
893 20. Maya-Martinez, R. *et al.* Recognition of peptidoglycan fragments by the transpeptidase Pbp4 from
894 *Staphylococcus aureus*. *Front. Microbiol.* **9**, 3223 (2019).
895 21. Sattler, M. Heteronuclear multidimensional NMR experiments for the structure determination of
896 proteins in solution employing pulsed field gradients. *Progress in Nuclear Magnetic Resonance*
897 *Spectroscopy* **34**, 93–158 (1999).
898 22. Harz, H., Burgdorf, K. & Höltje, J.-V. Isolation and separation of the glycan strands from murein of
899 *Escherichia coli* by reversed-phase high-performance liquid chromatography. *Analytical*
900 *Biochemistry* **190**, 120–128 (1990).
901 23. Gonzalez-Delgado, L. S. *et al.* Two-site recognition of *Staphylococcus aureus* peptidoglycan by
902 lysostaphin SH3b. *Nat Chem Biol* **16**, 24–30 (2020).

903 24. Caparrós, M., Pisabarro, A. G. & de Pedro, M. A. Effect of D-amino acids on structure and
904 synthesis of peptidoglycan in *Escherichia coli*. *J Bacteriol* **174**, 5549–5559 (1992).
905 25. Lam, H. *et al.* D-amino acids govern stationary phase cell wall remodeling in bacteria. *Science* **325**,
906 1552–1555 (2009).
907 26. Basler, M., Pilhofer, M., Henderson, G. P., Jensen, G. J. & Mekalanos, J. J. Type VI Secretion
908 requires a dynamic contractile phage tail-like structure. *Nature* **483**, 182–186 (2012).
909 27. Vollmer, W., Joris, B., Charlier, P. & Foster, S. Bacterial peptidoglycan (murein) hydrolases. *FEMS*
910 *Microbiol Rev* **32**, 259–286 (2008).
911 28. Daly, K. E., Huang, K. C., Wingreen, N. S. & Mukhopadhyay, R. Mechanics of membrane bulging
912 during cell-wall disruption in Gram-negative bacteria. *Phys. Rev. E* **83**, 041922 (2011).
913 29. Ursinus, A. *et al.* Murein (peptidoglycan) binding property of the essential cell division protein FtsN
914 from *Escherichia coli*. *J Bacteriol* **186**, 6728–6737 (2004).
915 30. Koch, A. L. Additional arguments for the key role of “smart” autolysins in the enlargement of the wall
916 of Gram-negative bacteria. *Research in Microbiology* **141**, 529–541 (1990).
917 31. Kari, J., Andersen, M., Borch, K. & Westh, P. An inverse Michaelis–Menten approach for interfacial
918 enzyme kinetics. *ACS Catal.* **7**, 4904–4914 (2017).
919 32. Terry, B. J., Jack, W. E. & Modrich, P. Facilitated diffusion during catalysis by EcoRI endonuclease.
920 Nonspecific interactions in EcoRI catalysis. *Journal of Biological Chemistry* **260**, 13130–13137
921 (1985).
922 33. Stracy, M. *et al.* Transient non-specific DNA binding dominates the target search of bacterial DNA-
923 binding proteins. *Molecular Cell* **81**, 1499-1514.e6 (2021).
924 34. Broendum, S. S. *et al.* High avidity drives the interaction between the streptococcal C1 phage
925 endolysin, PlyC, with the cell surface carbohydrates of Group A *Streptococcus*. *Mol Microbiol* **116**,
926 397–415 (2021).

927 35. McLaren, A. D. & Packer, L. Some aspects of enzyme reactions in heterogeneous systems. in
928 *Advances in enzymology and related areas of molecular biology* (ed. Nord, F. F.) vol. 33 245–308
929 (Interscience Publishers, 1970).
930 36. Grosdidier, A., Zoete, V. & Michielin, O. SwissDock, a protein-small molecule docking web service
931 based on EADock DSS. *Nucleic Acids Research* **39**, W270–W277 (2011).
932 37. Stankeviciute, G. *et al.* Differential modes of crosslinking establish spatially distinct regions of
933 peptidoglycan in *Caulobacter crescentus*. *Mol Microbiol* **111**, 995–1008 (2019).
934 38. Delaglio, F. *et al.* NMRPipe: A multidimensional spectral processing system based on UNIX pipes.
935 *J Biomol NMR* **6**, (1995).
936 39. Johnson, B. A. & Blevins, R. A. NMR View: A computer program for the visualization and analysis
937 of NMR data. *J Biomol NMR* **4**, 603–614 (1994).
938 40. Downing, A. K. *Protein NMR Techniques*. (Humana Press, 2004).
939 41. Frank, O., Kreissl, J. K., Daschner, A. & Hofmann, T. Accurate determination of reference materials
940 and natural isolates by means of quantitative ^{1}H NMR spectroscopy. *J. Agric. Food Chem.* **62**,
941 2506–2515 (2014).
942 42. Favier, A. & Brutscher, B. Recovering lost magnetization: polarization enhancement in biomolecular
943 NMR. *J Biomol NMR* **49**, 9–15 (2011).
944 43. Guzman, L. M., Belin, D., Carson, M. J. & Beckwith, J. Tight regulation, modulation, and high-level
945 expression by vectors containing the arabinose P_{BAD} promoter. *J Bacteriol* **177**, 4121–4130 (1995).
946 44. Mavor, D. *et al.* Determination of ubiquitin fitness landscapes under different chemical stresses in a
947 classroom setting. *eLife* **5**, e15802 (2016).
948 45. Hayes, B. M. *et al.* Ticks resist skin commensals with immune factor of bacterial origin. *Cell* **183**,
949 1562-1571.e12 (2020).
950 46. Stover, C. K. *et al.* Complete genome sequence of *Pseudomonas aeruginosa* PAO1, an
951 opportunistic pathogen. *Nature* **406**, 6 (2000).

952 47. MacDowell, A. A. *et al.* Suite of three protein crystallography beamlines with single superconducting
953 bend magnet as the source. *J Synchrotron Rad* **11**, 447–455 (2004).
954 48. Emsley, P. & Cowtan, K. *Coot*: model-building tools for molecular graphics. *Acta Crystallogr D Biol*
955 *Crystallogr* **60**, 2126–2132 (2004).
956 49. Adams, P. D. *et al. PHENIX*: a comprehensive Python-based system for macromolecular structure
957 solution. *Acta Crystallogr D Biol Crystallogr* **66**, 213–221 (2010).
958 50. Davis, I. W., Murray, L. W., Richardson, J. S. & Richardson, D. C. MOLPROBITY: structure
959 validation and all-atom contact analysis for nucleic acids and their complexes. *Nucleic Acids*
960 *Research* **32**, W615–W619 (2004).
961 51. Pettersen, E. F. *et al.* UCSF Chimera - A visualization system for exploratory research and
962 analysis. *J. Comput. Chem.* **25**, 1605–1612 (2004).
963